New scenario of plasma evolution in IC 443

Arisa HIRAYAMA,[1,*] Shigeo YAMAUCHI,[1] Kumiko K. NOBUKAWA,[1]
Masayoshi NOBUKAWA,[2] and Katsuji KOYAMA[3]

[1]Department of Physics, Nara Women's University, Kitauoyanishimachi, Nara, Nara 630-8506, Japan
[2]Faculty of Education, Nara University of Education, Takabatake-cho, Nara, Nara 630-8528, Japan
[3]Department of Physics, Graduate School of Science, Kyoto University, Kitashirakawa-oiwake-cho, Sakyo-ku, Kyoto, Kyoto 606-8502, Japan

*E-mail: raa_hirayama@cc.nara-wu.ac.jp

Abstract

Most young and middle-aged supernova remnants (SNRs) exhibit an ionizing plasma (IP), an ionizing process following a shock-heated SNR gas. On the other hand, significant fractions of SNRs exhibit a recombining plasma (RP). The origin and the mechanisms of the RP, however, are not yet well understood. This paper proposes a new model that the RP follows after the IP process taken at the first epoch of the SNR evolution. Using the high-quality and wide-band (0.6–10 keV) spectrum of IC 443, we fitted it with a model of two RPs (two-RP model) plus a power law (PL) with an Fe I Kα line component. The ionization temperature in one RP monotonically increases from Ne–Ca, while that in the other RP shows a drastic increase from Cr–Ni. The origin and mechanism of the two-RP and PL with an Fe I Kα line components are possibly due to different evolution of two plasmas and ionization by low-energy cosmic rays.

Key words: ISM: individual (IC 443) — ISM: supernova remnants — X-rays: ISM

1 Introduction

The common concept of a shock-heated plasma in supernova remnants (SNRs) is that the electron temperature (kT_e) and ionization temperature (kT_i) are nearly ~ 0 keV (the atoms are nearly neutral) at the initial epoch. Soon after, kT_e increases quickly, and then gradually ionized atoms, or kT_i follows after kT_e. Thus the SNR plasma is not in collisional ionization equilibrium (CIE: $kT_e = kT_i$), but is an ionizing plasma (IP: $kT_e > kT_i$). Since the X-ray spectra of most of the young–middle-aged SNRs are well fitted with the IP model, IP is widely accepted to be a standard SNR evolution (hereafter, IP SNR). However, recently some SNRs have been shown to exhibit a recombining plasma (RP), $kT_e < kT_i$ (hereafter, RP SNR). Contrary to the clear physics of IP SNRs, the physics for the evolution of RP

SNRs or how to make $kT_e < kT_i$ plasma has so far been unclear.

IC 443 (G189.1+3.0) is an SNR with a diameter of 45′ at a distance of 1.5 kpc (e.g., Welsh & Sallmen 2003). In the X-ray band, the age is estimated to be 3000–30000 yr (e.g., Petre et al. 1988; Olbert et al. 2001), a middle-aged–old SNR. It is also reported as a core collapsed (CC-SNR) and mixed morphology SNR (MM-SNR: Rho & Petre 1998). A hint of RP was discovered in the IC 443 spectrum for the first time by Kawasaki et al. (2002). Yamaguchi et al. (2009) then discovered an enhanced structure of the radiative recombination continuum (RRC) of the He-like silicon (Si XIII) and sulfur (S XV), which were direct evidence for RP. The RRC of the He-like iron (Fe XXV), a key element of the evolution, was found from this middle-aged–old SNR

Table 1. Observation logs.

Obs. ID	Obs. date start time–end time	(RA, Dec)$_{J2000.0}$	Exposure (ks)
		IC 443	
501006010	2007-03-06 10:40:19–2007-03-07 12:22:14	($6^h17^m11^s$, $22°46'32''$)	42.0
507015010	2012-09-27 05:29:48–2012-09-29 18:40:22	($6^h17^m11^s$, $22°45'12''$)	101.8
507015020	2013-03-27 04:15:06–2013-03-28 16:00:19	($6^h17^m12^s$, $22°44'47''$)	59.3
507015030	2013-03-31 11:44:34–2013-04-03 21:12:21	($6^h17^m12^s$, $22°44'46''$)	131.2
507015040	2013-04-06 05:21:49–2013-04-08 02:00:21	($6^h17^m12^s$, $22°44'52''$)	75.6
		Background	
409019010	2014-10-05 15:12:56–2014-10-07 19:09:17	($6^h27^m15^s$, $14°53'24''$)	82.1

in the limited energy band of 3.7–10 keV (Ohnishi et al. 2014). The RRC structures of these key elements play a key role in investigating the spectral evolution of RP SNRs. We have therefore made a deep observation of IC 443 with Suzaku (Mitsuda et al. 2007) to establish the RP structures in many key elements.

Conventionally, a model of the RP process is treated as starting from a common kT_i in all the elements. We propose a new model of the RP, which starts from element-dependent $kT_i(z)$. To verify this new model, and to combine the RP with the well-established IP process, we utilize the 0.6–10 keV spectrum of IC 443 obtained in ∼400 ks exposure observations with Suzaku. Details of the new RP model, the analysis process, and the results are presented in section 3. Based on the results, the implications for the RP origin in IC 443 are discussed in section 4. The quoted errors are in the 90% confidence limits.

2 Observations

The Suzaku observations of IC 443 were performed with the X-ray Imaging Spectrometer (XIS: Koyama et al. 2007) placed at the focal planes of the thin foil X-ray Telescopes (XRT: Serlemitsos et al. 2007). The XIS consists of four sensors. One of the XIS (XIS 1) is a back-side illuminated (BI) CCD, while the other three XIS sensors (XIS 0, 2, and 3) are front-side illuminated (FI) CCDs. In order to achieve the highest count rate ratio of IC 443/NXB (non-X-ray background) in the higher-energy band, we only used the FI, following Ohnishi et al. (2014). The count rate ratio of IC 443/NXB is determined by the count rates of IC 443 and NXB. The FI and BI photon count rate ratios of IC 443 are estimated by their quantum efficiencies, and are ∼1.5–1.8 in the Fe XXVI Lyα and RRC energy band of 7–10 keV (see figure 4 of Koyama et al. 2007), while the count rate ratio of NXB is ∼0.3–0.06 (see figure 16 of Koyama et al. 2007). As a matter of fact, the observed IC 443 FI and BI photon count rates are 3.0×10^{-3} counts s^{-1} and 1.5×10^{-3} counts s^{-1}, while the count rates for NXB are 1.56×10^{-2} counts s^{-1}

and 6.44×10^{-2} counts s^{-1}, respectively. Therefore, the FI count rate ratio of IC 443/NXB is ∼0.2, about 10 times better than that of BI: ∼0.02. Accordingly, we only use the FI in the analysis of the high-energy band of 7–10 keV. The count rate ratio of IC 443/NXB being worse for BI than FI is mainly attributable to the larger NXB count rate of BI than FI. The data used in this paper are listed in table 1.

The XIS was operated in the normal clocking mode. The field of view (FOV) of the XIS is $17\rlap{.}'8 \times 17\rlap{.}'8$. The XIS employed the spaced-row charge injection (SCI) technique to recover the spectral resolution (Uchiyama et al. 2009). The XIS data in the South Atlantic Anomaly, during Earth occultation, and at the low elevation angle from the Earth rim of <5° (night Earth) and <20° (day Earth) were excluded. Removing hot and flickering pixels, data of Grades 0, 2, 3, 4, and 6 were used. The XIS pulse-height data were converted to pulse-invariant (PI) channels using the xispi software in HEAsoft 6.19 and the calibration database version 2016-06-07. We used only XIS 0 and XIS 3 after 2006 November because XIS 2 became non-functional after the epoch. A small fraction of the XIS 0 area became unavailable, possibly due to a micro-meteorite impact, on 2009 June 23. After the epoch, we ignore the damaged area of the XIS 0.

3 Analysis and results

3.1 X-ray image

X-ray photons of IC 443 were taken from the data in the observations listed in table 1 (rows 1–5). After subtraction of the NXB generated by xisnxbgen (Tawa et al. 2008), the X-ray images in the 2.2–5.2 keV (color map) and 5.5–10 keV (green contour) bands are shown in figure 1, where the calibration source regions are excluded. These energy bands were selected from ejecta-dominant plasma (see figures 3c and d). In comparison with diffuse structure in the 2.2–5.2 keV band, the 5.5–10 keV-band image shows clear concentration toward the image center (the
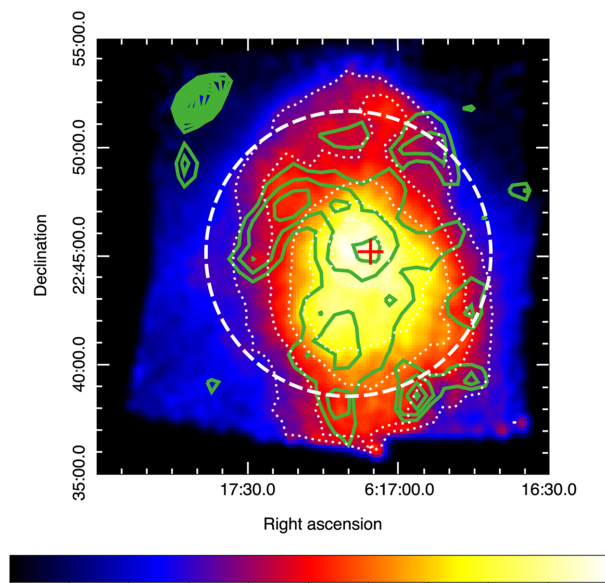
Fig. 1. X-ray map of the main part of IC 443 in the 2.2–5.2 keV (color image and white dotted line, RP1) and 5.5–10 keV (contour image, RP2) bands, with NXB substraction and vignetting correction. The coordinates are J2000.0. The scales are linear (peak to bottom). The red cross shows a peak of the RP2 component. The IC 443 spectrum is taken from the white dashed circle. The bright source in the 5.5–10 keV band at the upper left is an unrelated point source (No. 9 in table 2 of Bocchino & Bykov 2003). (Color online)

cross mark). This contrast would be closely related to the two-component spectral structure found in subsection 3.4.

3.2 Overview of the RP process

In contrast to the well-established IP SNR scenario, that of RP SNRs has not been established yet. In this paper, we propose a viable scenario based on the standard IP SNR evolution; the RP process follows after the IP process. Figure 2 illustrates the scenario of the spectral evolution of SNRs, and how RP follows after IP.

Phase 1 (IP process) The SNR evolution starts by a shock-heating, in which kT_i and kT_e are nearly 0 keV. kT_e quickly increases to several keV, which gradually ionizes neutral atoms, and hence kT_i also gradually increases following kT_e (phase 1). Thus, phase 1 is the ionizing plasma (IP) process of $kT_e > kT_i$. To evolve into the next phase (phase 2) of the RP process of $kT_e < kT_i$, there should be a transition phase as shown by epochs A and B in figure 2. In this transition phase, kT_e drops below kT_i, by either conductive cooling by cold cloud (conduction: Kawasaki et al. 2002) or adiabatic cooling by break-out of the plasma from a dense medium to a thin medium (rarefaction: Masai 1994)— see figure 2a. The other possibility is that kT_i increases by either photo-ionization of an external X-ray source or ionization by

low-energy cosmic rays (LECRs, e.g., Nakashima et al. 2013)— see figure 2b.[1]

Phase 2 (RP process) After the transition, SNR evolution enters the RP process, in which free electrons at the lower temperature of kT_e are recombining to bound states of ions at the higher ionization temperature of kT_i. This process makes an RRC. The RRC structure is direct evidence for RP, and has been clearly observed in Si and S in IC 443 (Yamaguchi et al. 2009). As noted in section 1, the conventional model of RP SNRs ignores the phase 1 process and considers only the phase 2 process: RP starts from a plasma with $kT_i > kT_e$, where kT_i are all the same in the relevant elements at epoch B (here, single-kT_i). Our new model explicitly assumes element-dependent $kT_i(z)$ [here, multi-$kT_i(z)$ model], which can be smoothly connected to the IP (phase 1), a well-established process for almost all SNRs.

A multi-$kT_i(z)$ model fit has been partially applied to the RP analysis of W 28 in a limited energy band (0.6–5 keV) with relevant elements of Ne–Fe (Sawada & Koyama 2012). For a more comprehensive multi-$kT_i(z)$ model fit of IC 443 than those of the W 28 study, we utilized the wider energy band spectrum of 0.6–10 keV. This energy band covers essentially all the relevant elements from Ne to Ni.

3.3 Outline of analysis

The spectrum of the background (BGD) was extracted from the nearby sky region; the model spectrum is based on Masui et al. (2009), which consisted of the Milky Way halo (MWH), the local hot bubble (LHB), and the cosmic X-ray background (CXB; Kushino et al. 2002). For the study of the spectra and fluxes of IC 443, we used the data within a circle of $6'.5$ radius centered on (RA, Dec)$_{J2000.0}$ = ($6^h17^m10^s.000$, $+22°45'10''.00$), excluding calibration sources. IC 443 is located at the anti-center region with a Galactic latitude of $b = 3°$, and hence the Galactic ridge X-ray emission (GRXE) is ignored (Uchiyama et al. 2013; Yamauchi et al. 2016; Koyama 2018). Since we found an Fe I Kα line, which should be associated with a continuum, we added a power-law component (PL) with an Fe I Kα line.

Thus, the formula of the spectral fitting is the sum of plasma from the interstellar medium (ISM) and SNR ejecta (Ejecta), a power law (PL) plus Fe I Kα line [Gaussian

---

[1] Depending on the transition process, the duration (A→B) is not always as short as in figure 2. In some cases (LECR origin), its duration is very long, extending from the initial to the present epoch.

(a)   (b)
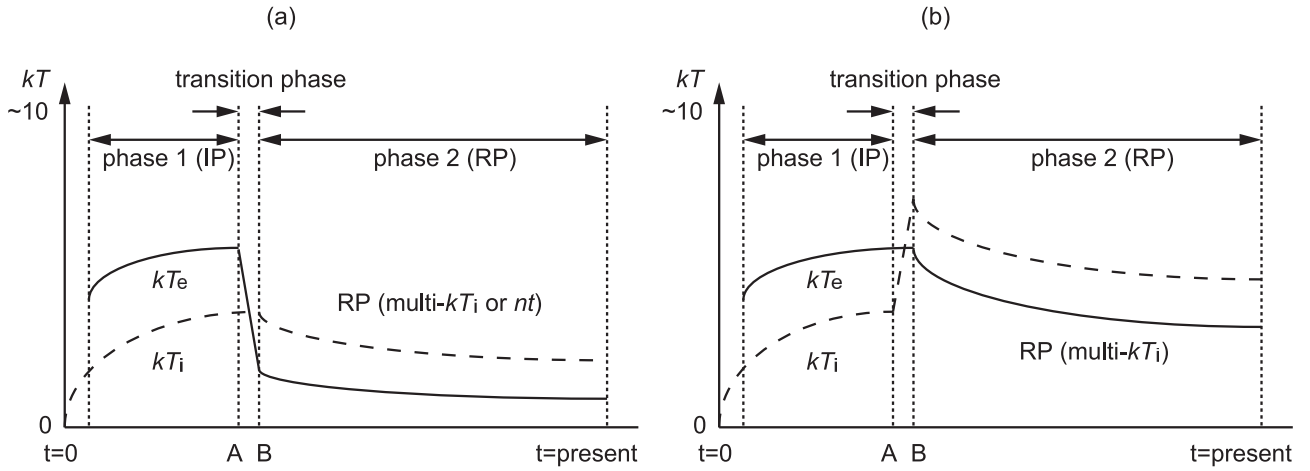
Fig. 2. Schematic pictures of the kT_e and kT_i evolutions in an RP SNR. (a) is the case where the electron temperature (kT_e) decreases, and (b) is the case where the ionization temperature (kT_i) increases.

(6.4 keV)], and the nearby X-ray background (BGD). This is given as

$$ISM + Ejecta + PL + Gaussian(6.4\,keV) + BGD. \qquad (1)$$

The ejecta plasma model (Ejecta) is either single-kT_i (conventional model) or multi-$kT_i(z)$ (new model) in the VVRNEI code of the XSPEC package (version 12.9.1). The latter is given as

$$\sum_{z=H}^{z=Ni} VVRNEI[\text{multi-}kT_i(z)], \qquad (2)$$

where $kT_i(z)$ is the variable ionization temperature for each element. We added two Gaussians at $\sim$0.8 keV and $\sim$1.2 keV to represent the features due to incomplete atomic data for the Fe-L shell complex in the current plasma model (e.g., Nakashima et al. 2013).

As shown in table 1, the observations extended over a large time span. Although the energy resolution in the first observation was not degraded by a particle background, those of the latter observations were significantly degraded. In order to compensate for these energy resolution variations in the summed spectrum, we applied the gsmooth code from XSPEC. The line broadening due to the time-dependent variations of the energy resolution is $\sim$30 eV (FWHM). The energy scale was fine-tuned by applying an artificial redshift for every element. The gain variation with energy is a concaved function with the amplitude of $+1.4\%$–-0.4% in redshift.

3.4 RP model fit

Model A At first, we fitted the IC 443 spectrum using equation (1) of the single-kT_i model (RP1) for the ejecta

spectrum (Ejecta). The free parameters were N_H, kT_e, kT_i [$kT_i(z)$], the recombination timescale ($n_e t$), the normalizations, and the abundances of Ne–Ni, while the abundances of He, C, N, and O were assumed to be 1 solar. The abundance tables and the atomic data of the lines and continua of the thin thermal plasma were taken from Anders and Grevesse (1989) and ATOMDB 3.0.7, respectively.

The best-fit kT_e for the ISM is $\sim$0.2 keV, for which there is no significant difference between CIE and non-equilibrium ionization (NEI). We therefore assume that the ISM is CIE with the solar abundance (see, e.g., Matsumura et al. 2017). The global fit is rejected with a large χ^2/d.o.f. of 2473/938 (2.64).

Model B Next, we fitted with the multi-$kT_i(z)$ model (RP1) of equation (2). The free parameters were the same as model A. The global fit was significantly improved, with a χ^2/d.o.f. of 2007/932 (2.15). However, we found significant residuals in the 5–10 keV band, in particular at the Fe I Kα (6.4 keV), Fe XXV Heα (6.7 keV), and Ni VVVII Heα (7.8 keV) lines, and at the RRC of Fe XXV (8.83 keV).

Model C We therefore added another VVRNEI model (RP2) and a PL component. The VVRNEI model (RP2) is closely related to the Heα and Lyα lines of Cr–Ni. The normalization and the recombination timescale for RP2 were linked to those of the lower-temperature component (RP1). The PL component was associated with an Fe I Kα line. We could not constrain the photon index (Γ) value by the fitting. Non-thermal SNRs typically have a Γ of 2–3 (e.g., SN1006: Bamba et al. 2003, 2008; RX J1713−3946: Koyama et al. 1997). Accordingly, we assumed the power-law index Γ to be 2.5. The line width was assumed to be 0 keV. The global fit was largely improved, with a χ^2/d.o.f. of 1674/923 (1.81). From the
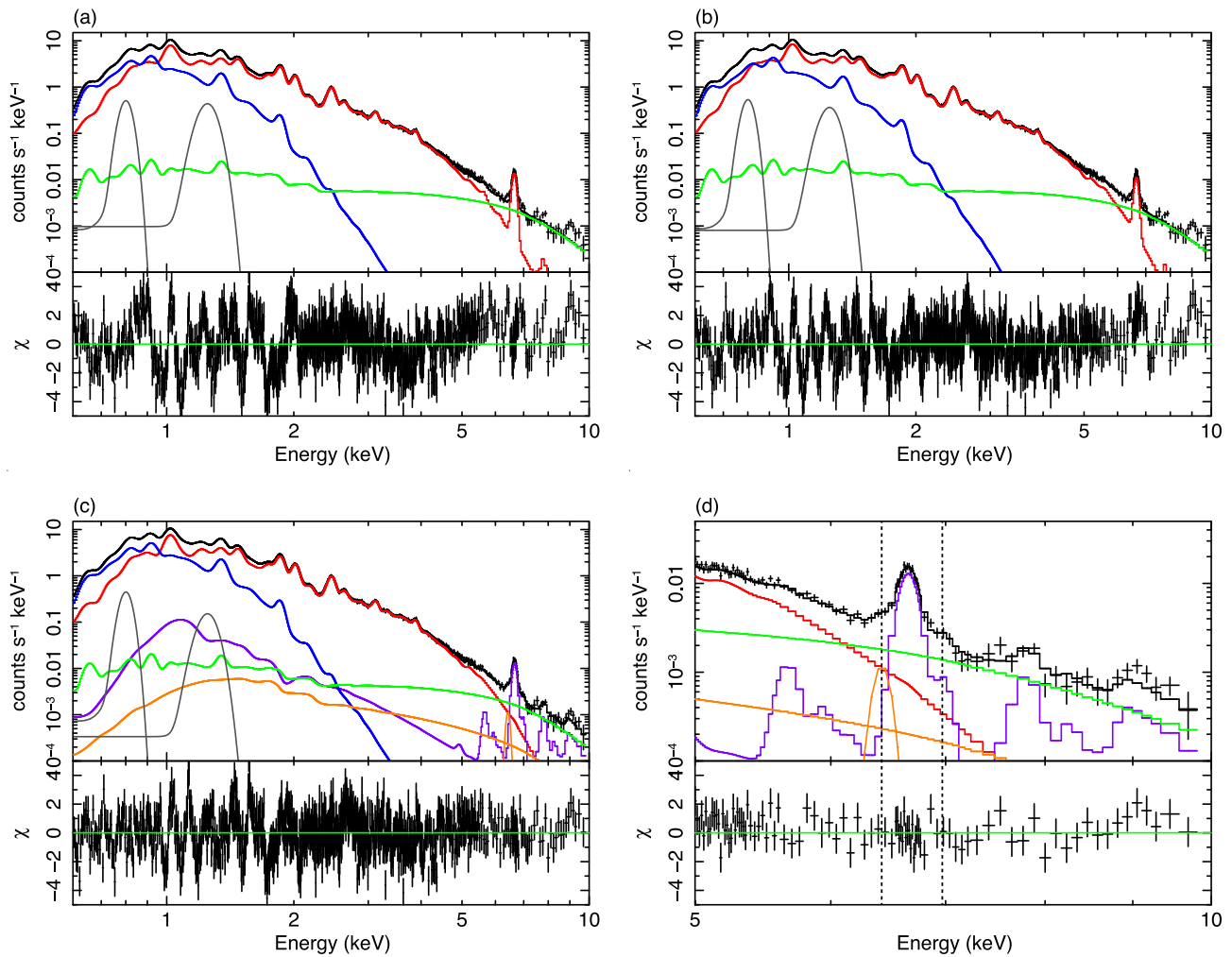
Fig. 3. XIS spectrum of IC 443 and the best-fit models: (a) single-kT_i (model A), (b) multi-$kT_i(z)$ (model B), (c) two-RP of multi-$kT_i(z)$ (model C), and (d) same as (c) but in the 5–10 keV band. The solid red, purple, blue, and orange lines are RP1, RP2, CIE, and PL plus an Fe I $K\alpha$ line, respectively. The gray lines show Fe-L lines, while the green line shows the BGD (= MWH + LHB + CXB). The dotted lines in (d) indicate data excess at the energies of the Fe I $K\alpha$ (left) and Fe XXVI Lyα lines (right). (Color online)

pure statistical point of view, model C is still unacceptable. However, possible errors, such as atomic data of L-lines of Fe XVI and Fe XVIII, and small calibration errors near the Si I K-edge energy, may not be negligible for a spectrum with very high photon statistics. The actual photon count rate in the Si K-edge band (1.83–1.85 keV) was $(4.20 \pm 0.02) \times 10^{-2}$ counts s^{-1}.

Taking account of these systematic errors, we use the model C results as a reasonable approximation. The best-fit spectra of models A, B, and C are given in figure 3, while the best-fit parameters of models A, B, and C are listed in table 2. $kT_i(z)$ monotonically increases with z in Ne–Ca, then decreases in Cr–Ni for the RP1 component. The abundances of Ne–Ni are generally moderate. Some fractions of the Cr–Ni plasma (RP2) show a drastic increase of $kT_i(z)$.

In the Cr–Ni plasma, the abundance ratio of Ni/Fe is ∼5, but the abundances of Cr–Ni are very small.

4 Discussion

4.1 Two-RP model and its implication

The IC 443 spectrum is nicely fitted by a two-RP (RP1 and RP2) multi-$kT_i(z)$ model. The best-fit kT_e of RP1 and RP2 are 0.56 and 0.64 keV, respectively. Matsumura et al. (2017) also obtained a nice fit with a similar two-RP model for IC 443. However, their best-fit kT_e are 0.24 and 0.61 keV, respectively, largely different from our best-fit model. The best-fit abundances are also about two times larger than ours. We note that Matsumura et al. (2017) used a limited data set from ID = 501006010 (table 1)

Table 2. Best-fit parameters of single-kT_i (model A), multi-$kT_i(z)$ (model B), two-RP of multi-$kT_i(z)$ (model C), and two-RP of multi-$kT_i(z)$ in the CC-SNR case (model D).

Parameter					Values			
	Model A		Model B		Model C		Model D	
				— Absorption —				
N_H*	0.65 ± 0.01		0.65 ± 0.01		0.67 ± 0.01		0.67 ± 0.01	
				— ISM (CIE) —				
kT_e[†]	0.22 ± 0.01		0.21 ± 0.01		0.22 ± 0.01		(=model C)	
VEM[‡]	1.7 ± 0.7		1.8 ± 0.1		2.0 ± 0.1		(=model C)	
				— Ejecta (RP1) —				
kT_e[†]	0.53 ±0.01		0.53 ± 0.01		0.56 ± 0.01		(=model C)	
VEM[‡]	0.47 ± 0.02		0.54 ± 0.03		0.46 ± 0.04		0.042 ± 0.001	
$n_e t$[§]	3.6 ± 0.1		2.9 ± 0.2		2.0 ± 0.1		(=model C)	
	$kT_i(z)$[†]	Ab[‖]	$kT_i(z)$[†]	Ab[‖]	$kT_i(z)$[†]	Ab[‖]	$kT_i(z)$[†]	Ab[‖]
Ne	2.0 ± 0.1	2.9 ± 0.3	0.94 ± 0.12	2.6 ± 0.2	0.85 ± 0.05	3.4 ± 0.5	0.73 ± 0.02	34 ± 2
Mg	(link to Ne)	1.8 ± 0.2	1.1 ± 0.1	1.5 ± 0.1	1.1 ± 0.1	1.6 ± 0.1	(=model C)	19 ± 1
Al	(link to Ne)	2.2 ± 0.3	(link to Mg)	1.3 ± 0.2	(link to Mg)	1.1 ± 0.2	(=model C)	15 ± 2
Si	(link to Ne)	2.1 ± 0.2	1.7 ± 0.1	1.9 ± 0.1	1.5 ± 0.1	2.0 ± 0.2	(=model C)	22 ± 1
S	(link to Ne)	2.5 ± 0.2	1.7 ± 0.1	2.2 ± 0.1	1.6 ± 0.1	2.3 ± 0.2	(=model C)	26 ± 1
Ar	(link to Ne)	2.2 ± 0.3	1.9 ± 0.1	1.8 ± 0.2	1.6 ± 0.1	1.9 ± 0.2	(=model C)	21 ± 1
Ca	(link to Ne)	3.2 ± 0.4	3.9 ± 0.4	0.71 ± 0.10	2.7 ± 0.4	0.92 ± 0.22	(=model C)	10 ± 1
Cr=Mn	(link to Ne)	10 ± 3	(link to Fe)	12 ± 2	(link to Fe)	<0.4	(=model C)	<8
Fe	(link to Ne)	0.47 ± 0.29	1.4 ± 0.1	0.45 ± 0.02	0.81 ± 0.09	0.33 ± 0.03	(=model C)	3.8 ± 0.2
Ni	(link to Ne)	2.3 ± 0.2	(link to Fe)	1.7 ± 0.2	(link to Fe)	2.3 ± 0.2	(=model C)	28 ± 2
				— Ejecta (RP2) —				
kT_e[†]	—		—		0.64±0.11		(=model C)	
VEM[‡]	—		—		0.46 (link to RP1)		0.042 (link to RP1)	
$n_e t$[§]	—		—		2.0 (link to RP1)		(=model C)	
					kT_i[†]	Ab[‖]	kT_i[†]	Ab[‖]
Cr	—	—	—	—	(link to Fe)	0.30 ± 0.17	(link to Fe)	3.4 ± 1.6
Mn	—	—	—	—	(link to Fe)	<0.5	(link to Fe)	<5.0
Fe	—	—	—	—	6.2 ± 0.4	0.030 ± 0.003	(=model C)	0.33 ± 0.02
Ni	—	—	—	—	(link to Fe)	0.16 ± 0.10	(link to Fe)	1.7 ± 1.0
				— PL —				
Γ[♯]	—		—		2.5 (fixed)		2.5 (fixed)	
$Norm$[♯]	—		—		$7.8^{+10.1}_{-2.8}$		(=model C)	
				— Gaussian —				
E**	—		—		6.43±0.04		(=model C)	
$F_{6.4keV}$**	—		—		6.7±3.0		(=model C)	
χ^2/d.o.f.	2473/938 = 2.64		2007/932 = 2.15		1674/923 = 1.81		1722/941 = 1.83	

*The units are $\times 10^{22}$ cm^{-2}.

[†]Units of kT_e and $kT_i(z)$ are keV.

[‡]Volume emission measure (VEM = $n_e n_H V$) with a distance of 1.5 kpc. The units are 10^{58} cm^{-3}.

[§]Recombination timescale, where n_e is the electron density (cm^{-3}) and t is the elapsed time (s). The units are $\times 10^{11}$ cm^{-3} s.

[‖]Relative to the solar values in Anders and Grevesse (1989).

[♯]Power-law index and flux normalization. The units of normalization are 10^{-7} photons s^{-1} cm^{-2} keV^{-1} arcmin^{-2} at 1 keV.

**The Fe I Kα line energy and photon flux in units of keV and 10^{-9} photons s^{-1} cm^{-2} arcmin^{-2}, respectively.

and a limited energy band of 0.6–7.5 keV. We therefore refitted their model to our higher-quality data (includes all the Obs. ID in table 1) in the wider energy band (0.6–10 keV) to include the RRC of Fe. Then, the fit is rejected with χ^2/d.o.f. = 3589/926 = 3.88, which is larger than our simpler model A of one kT_e and one kT_i of

χ^2/d.o.f. = 2473/938 = 2.64. We also compare our best-fit results with the other previous IC 443 report, and find that model C is the best in reliability and quantity.

In the multi-$kT_i(z)$ model (model C) of ejecta, we found that the derived $kT_i(z)$ for each element is not the same, but shows monotonic increase in Ne–Ca and decrease in

Cr–Ni for RP1 (table 2). Since RP2 has different electron and ionization temperatures from those of RP1, the RP2 plasma may have a different origin. The RP2 component shows a higher Ni abundance than Fe (table 2), and might be dominated by spectrally hard emission concentrated in the central region of the SNR. Although this is speculative, this hard component emission appears to involve X-ray emission from elongated regions connected to the brightest SNR center (the green contours in figure 1) in contrast to the largely smooth distribution of the spectrally softer RP1 component (the dotted contours in figure 1). We speculate that the RP2 component emission might be associated with strong outflows of neutron-rich gas in the deepest core of the CC-SN. Deep follow-up high-resolution X-ray imaging spectroscopic observations of this central region of IC 443 would be required to test this scenario.

In models A–C (table 2), we fitted the ejecta plasma with fixed abundances of He–O of 1 solar, because these elements do not explicitly appear in the spectrum of $\gtrsim 0.7$ keV. Since CC-SNRs are largely over-solar abundances of He–O, we refitted the abundances for the case of He$\sim$2.6, C$\sim$6.4, N$\sim$6.5, and O$\sim$28 solar (model D), the mean values of Woosley and Weaver (1995). The results are given in table 2. The refitted abundances in RP1 are about 10 times larger than those of model C. The very small abundances of Fe and Ni in RP2 of model C increase to $\sim$0.3 and $\sim$1.7 solar in model D, respectively. The abundances for individual elements and their distribution in the RP1 and RP2 plasma are roughly consistent with the initial assumption of CC-SNR (e.g., Woosley & Weaver 1995).

From the kT_i given in table 2, the ionization temperature of Si and S in IC 443 is estimated to be $\sim$1.5 keV at the start of the RP process (epoch A in figure 2). This temperature gives significant Si XIV Lyα and S XVI Lyα, as shown in figure 3c. We checked the available SNR spectra with similar kT_e of IC 443 ($kT_e \sim 0.3$–1 keV), but found no significant Si XIV Lyα or S XVI Lyα from the IP SNR samples (e.g., Cygnus loop: Uchida et al. 2011; G272.2−3.2: Kamitsukasa et al. 2016; Kes 79: Sato et al. 2016). As for Fe XXVI Lyα, the IP SNR samples are limited, but a good sample is Cas A, which shows no Fe XXVI Lyα ($kT_e = 1$–2 keV, Hwang & Laming 2012). On the other hand, all the spectra of the RP SNR samples that correspond to phase 2 (after the transition of IP→RP) have clear Si XIV Lyα and S XVI Lyα (e.g., W 28: Sawada & Koyama 2012; G359.1−0.1: Ohnishi et al. 2011). Some RP SNRs with better statistics such as IC 443 (this paper) and W 49 B (Ozawa et al. 2009) show a clear Fe XXVI Lyα line. Since all the RP SNRs would be made by the transition of IP→RP (phase 1→phase 2), the observed Si XIV Lyα, S XVI Lyα, and Fe XXVI Lyα in IC 443 should be made by this transition.

The conventional model of electron cooling (figure 2a) does not increase the ionization temperature to make significant Si XIV Lyα, S XVI Lyα, or Fe XXVI Lyα lines, and hence cannot change the IP to RP in the transition phase. The electron cooling by thermal conduction to cool clouds has another problem: the ionization temperature would also decrease by contamination of cloud evaporation, and hence the plasma becomes IP, not RP, in the transition phase of figure 2a. Therefore, we rather prefer the model of ionization temperature increase shown in figure 2b, in which the ionization temperature at epoch B can be high enough to make Lyα lines of Si, S, and Fe, and Fe-RRC. The underlying process would be irradiation by external X-rays or LECRs.

We discovered an Fe I Kα line (6.4 keV) associated with a PL component. In order to explain both the RP and the Fe I Kα line, we propose a new model which is out of the standard scheme of SNR evolution. LECRs are successively produced by the SNR shock. They irradiate the SNR hot plasma and nearby cold cloud. Fe XXV in the hot plasma is ionized to Fe XXVI, then free electrons with a temperature of $\sim$0.6–0.7 keV in the hot plasma are recombined to the ground state of Fe XXVI after a long recombination process of $(2.0 \pm 0.1) \times 10^{11}$ cm^{-3} s. This process makes the Fe-RRC structure. For the origin of the Fe I Kα line, one may argue that the origin is irradiation of the molecular cloud by an external X-ray source. However, this is remote possibility, because no bright X-ray source is found near IC 443. We propose another possibility: the origin of the Fe I Kα plus continuum is due to LECRs. Our speculation, therefore, is that LECRs are successively produced by the SNR shock, and irradiate both the SNR hot plasma (responsible for RP) and nearby cold cloud (responsible for PL plus Fe I Kα).

4.2 A possible problem with the RP code

Model C, including VVRNEI in XSPEC, cannot fully explain the fluxes of Fe XXV Heα, Fe XXVI Lyα, and Fe XXV-RRC in the RP2 spectrum (see the 5–10 keV band in figure 3d) in IC 443; the observed flux ratio of RRC/Heα is larger than the code predicts. On the other hand, the RP code of SPEX for model C successfully reproduces the RRC/Heα ratio in the 3.7–10 keV band spectrum (Ohnishi et al. 2014). We therefore tried to refit the 5–10 keV band spectrum using the SPEX code of the latest version. Unlike the XSPEC code, this model using SPEX reproduces well the 5–10 keV-band spectrum, in particular the flux ratio of Fe-RRC/Fe XXV Heα. Thus, we confirm a problem of disagreement between XSPEC and SPEX. To investigate the origin of this code disagreement in the Suzaku spectrum is beyond the scope of this paper. The high-resolution calorimeter on

board the future mission of XRISM may solve this question, because it can resolve the fine structure of Fe Heα (x, y, z, and w) and Lyα1 and Lyα2. The absolute flux and the flux ratios of these fine-structure lines are essential for the basic atomic process in the RP and the other plasma processes in SNR.

5 Conclusions

We provide the IC 443 spectrum of the highest signal-to-noise ratio in the widest energy band of 0.6–10 keV. The analysis process and results for the unprecedented spectrum are given as follows:

- The multi-$kT_i(z)$ model of RP is nicely fitted to the IC 443 spectrum.
- The distribution of $kT_i(z)$ as z in Ne–Ca monotonically increases, then decreases in Cr–Ni. However, a fraction of Cr–Ni show a drastic increase.
- Cr XXIII Heα and Fe I Kα lines are found for the first time.
- The high abundance ratio of Ni/Fe may support that Ni is overproduced in the neutron-rich central region (in the neutron star).
- We interpret that the origin of the RP and an Fe I Kα line in IC 443 are enhanced ionization by irradiation of LECRs.

References

Anders, E., & Grevesse, N. 1989, Geochim. Cosmochim. Acta, 53, 197
Bamba, A., et al. 2008, PASJ, 60, S153
Bamba, A., Yamazaki, R., Ueno, M., & Koyama, K. 2003, ApJ, 589, 827
Bocchino, F., & Bykov, A. M. 2003, A&A, 400, 203
Hwang, U., & Laming, M. 2012, ApJ, 746, 130
Kamitsukasa, F., Koyama, K., Nakajima, H., Hayashida, K., Mori, K. Katsuda S., Uchida, H., & Tsunemi, H. 2016, PASJ, 68, S7
Kawasaki, M. T., Ozaki, M., Nagase, F., Masai, K., Ishida, M., & Petre, R. 2002, ApJ, 572, 897
Koyama, K. 2018, PASJ, 70, R1
Koyama, K., et al. 2007, PASJ, 59, S23
Koyama, K., Kinugasa, K., Matsuzaki, K., Nishiuchi, M., Sugizaki, M., Torii, K., Yamauchi, S., & Aschenbach, B. 1997, PASJ, 49, L7
Kushino, A., Ishisaki, Y., Morita, U., Yamasaki, N. Y., Ishida, M., Ohashi, T., & Ueda, Y. 2002, PASJ, 54, 327
Masai, K. 1994, ApJ, 437, 770
Masui, K., Mitsuda, K., Yamasaki, N. Y., Takei, Y., Kimura, S., Yoshino, T., & McCammon, D. 2009, PASJ, 61, S115
Matsumura, H., Tanaka, T., Uchida, H., Okon, H., & Tsuru, T. G. 2017, ApJ, 851, 73
Mitsuda, K., et al. 2007, PASJ, 59, S1
Nakashima, S., Nobukawa, M., Uchida, H., Tanaka, T., Tsuru, T. G., Koyama, K., Murakami, H., & Uchiyama, H. 2013, ApJ, 773, 20
Ohnishi, T., Koyama, K., Tsuru, T. G., Masai, K., Yamaguchi, H., & Ozawa, M. 2011, PASJ, 63, 527
Ohnishi, T., Uchida, H., Tsuru, T. G., Koyama, K., Masai, K., & Sawada, M. 2014, ApJ, 784, 74
Olbert, C. M., Clearfield, C. R., Williams, N. E., Keohane, J. W., & Frail, D. A. 2001, ApJ, 554, L205
Ozawa, M., Koyama, K., Yamaguchi, H., Masai, K., & Tamagawa, T. 2009, ApJ, 706, L71
Petre, R., Szymkowiak, A. E., Seward, F. D., & Willingale, R. 1988, ApJ, 335, 215
Rho, J., & Petre, R. 1998, ApJ, 503, L167
Sato, T., Koyama, K., Lee, S.-H., & Takahashi, T. 2016, PASJ, 68, S8
Sawada, M., & Koyama, K. 2012, PASJ, 64, 81
Serlemitsos, P. J., et al. 2007, PASJ, 59, S9
Tawa, N., et al. 2008, PASJ, 60, S11
Uchida, H., Tsunemi, H., Tominaga, N., Katsuda, S., Kimura, M., Kosugi, H., Takahashi, H., & Takakura, S. 2011, PASJ, 63, 199
Uchiyama, H., et al. 2009, PASJ, 61, S9
Uchiyama, H., Nobukawa, M., Tsuru, T. G., & Koyama, K. 2013, PASJ, 65, 19
Welsh, B. Y., & Sallmen, S. 2003, A&A, 408, 545
Woosley, S. E., & Weaver, T. A. 1995, ApJ, 101, 181
Yamaguchi, H., Ozawa, M., Koyama, K., Masai, K., Hiraga, J. S., Ozaki, M., & Yonetoku, D. 2009, ApJ, 705, L6
Yamauchi, S., Nobukawa, K. K., Nobukawa, M., Uchiyama, H., & Koyama, K. 2016, PASJ, 68, 59